Effect of 2 wt% Ag Addition on Corrosion Properties of ZK40 for Biodegradable Applications

M. AbdelGawad, B. Mansoor, M. W. Vaughan, and I. Karaman

Abstract

The antibacterial effects of silver make it an attractive alloying element for biodegradable Mg alloys to treat possible inflammation and infections caused by the degrading orthopedic implants. In this study, as-extruded Mg–4%Zn–0.5%Zr (ZK40) alloy was alloyed with Ag, specifically 2 wt%, and subjected to a heat treatment at 350 °C for 7 days. The mechanical and corrosion responses were studied in two orthogonal planes (transverse and extrusion) before and after silver addition to explore its potential for biodegradable orthopedic applications. Corrosion characteristics were assessed at 37 °C in Hank's solution for 24 h via electrochemical impedance spectroscopy (EIS), potentiodynamic polarization (PD) and open circuit potential (OCP). As-extruded and heat-treated ZK40 alloy displayed an inhomogeneous microstructure containing large, coarse grains, Zn–Zr rich secondary phase and some fine grain regions. While in ZK40–Ag, both planes showed a relatively more homogenous microstructure but with some agglomeration of Zn–Ag rich secondary phases. Here, we present our initial results on the different corrosion behaviors observed in the two materials.

M. AbdelGawad · B. Mansoor (✉)
Mechanical Engineering Program, Texas A&M University at Qatar, Doha, Qatar
e-mail: bilal.mansoor@qatar.tamu.edu

M. AbdelGawad · B. Mansoor · I. Karaman
Mechanical Engineering Department, Texas A&M University at Qatar, College Station, TX, USA

B. Mansoor · M. W. Vaughan · I. Karaman
Materials Science and Engineering Program, Texas A&M University at Qatar, College Station, TX, USA

Introduction

Temporary orthopedic implants are designed to restore the functionality of fractured load-bearing joints and bones by providing temporary support during the healing process. Biodegradable implants have attracted attention for decades now due to their superiority over permanent implants where they are able to sustain the joint/bone for the required duration and then progressively degrade afterwards. This eliminates the need for a second removal surgery which is inevitable when using permanent implants. Furthermore, permanent implants are associated with several lifelong problems such as prolonged physical irritation, chronic inflammation and endothelial dysfunction [1, 2]. Magnesium (Mg) alloys have proven to be promising candidates exhibiting excellent biocompatibility due to the presence of Mg which is an essential element in bone and soft tissue [3]. In addition, Mg and its alloys have elastic moduli (37.5–65 GPa) similar to that of the human bone (3–20 GPa) preventing the possibility of mechanical failure of the implant due to stress shielding or implant loosening [4]. Research has shown successful in vivo testing, in addition to clinical trials, where Mg-based implants helped stimulate the formation of new bone around the implantation site [3, 5, 6].

Biodegradable implants are designed to maintain their mechanical integrity while fulfilling their intended function. A major drawback that still prevents the commercialization of Mg-based orthopedic implants is their rapid degradation specifically at the early implantation stages where degradation is usually the fastest [6]. Uncontrollable degradation can lead to failure of the implant before the bone is completely healed as well as the excessive release of metallic ions beyond their toxicity limits [1]. Consequently, numerous design strategies have been proposed to develop biocompatible Mg alloys with sufficient strength and controllable corrosion characteristics [1, 4, 7, 8].

Most of the Mg alloys reported are based on commercial Mg alloys that were primarily developed for the

transportation and aerospace industry since they usually satisfy the required mechanical strength. Solution strengthening, grain size control and, precipitation hardening are all methods used on these commercially available alloys to tailor their corrosion behavior. In addition, efforts have been made to improve their mechanical and corrosion behavior through micro-alloying, heat treatments and/or severe plastic deformation [9–14]. Mg–Zn alloys have been studied extensively for biomedical applications since the two main constituents are Mg and Zinc (Zn) which are both essential nutrients for the human body and therefore biocompatible [15–20]. Chen et al. conducted in vitro and in vivo tests on Mg–Zn alloy using mouse pre-osteoblastic MC3T3-E1 cells and compared it with polymer poly-l-lactic acid (PLLA) implant and concluded that Mg–Zn alloy allowed for better cell attachment and mineralization as well as new bone formation [21]. In addition, previous work has been done by the authors using commercial Mg–Zn alloy with rare earth addition (ZE41 and EZ33) where their biodegradation characteristics were studied in Hank's solution and NaCl [22, 23]. In an attempt to investigate different alloying systems, Mg–Zn–Zr alloys (ZK series) were considered for this study since they are also potential candidates as biomaterials considering that Zirconium (Zr) is also a biocompatible element that is non-toxic to the human body in small amounts [24]. Furthermore, Zr is known to be an excellent grain refiner in Mg alloys and has been shown to improve its corrosion resistance when alloyed in small amounts <0.5 wt % [25].

On the other hand, Ag is known to have superior antibacterial effects and can be effective on some antibiotic-resilient microbes such as Methicillin-resistant Staphylococcus aureus (MRSA) [26]. Tie et al. developed three binary Mg–X Ag alloys (where X = 2, 4 and 6 wt%) and studied their mechanical and corrosion characteristics, as well in vitro cytocompatibility [26]. It was concluded that Ag improved the mechanical strength of Mg and that although the corrosion rate of the Mg increased with increasing addition of Ag, the susceptibility of Mg to pitting corrosion decreased. Localized corrosion has been reported to be more critical than uniform corrosion to the mechanical integrity of biodegradable materials owing to the accelerated loss of mechanical strength within a short period of time [27]. Furthermore, Ben-Hamu et al. studied the corrosion behavior and microstructural evolution of Mg–Zn–Ag alloys by varying the concentration of Ag between 0, 1, 2 and 3 wt

%Ag [28]. It was reported that the increasing addition of Ag resulted in an increased refinement of the grains and an increase in the hardness. However, an improvement in corrosion resistance was only witnessed when the Ag addition was up to 2 wt%Ag.

In this preliminary work, as-extruded ZK40 (Mg 95.0 wt %, Zn 4.5 wt%, Zr 0.5 wt%) was selected as a base material to investigate the effect of 2 wt% Ag addition (ZK40–Ag) on its mechanical properties and in vitro corrosion characteristics using Hank's solution at 37 °C. Microstructural analysis was performed on the as-extruded alloys before and after suitable heat-treatments. Mechanical testing was carried out by way of compression tests and Vicker's microhardness while corrosion response was accessed by employing electrochemical techniques such as Open Circuit Potential (OCP), Electrochemical Impedance Spectroscopy (EIS) and Potentiodynamic Polarization (PD).

Experimental Methods

Materials

ZK40 and ZK40–Ag ingots were produced by gravity die casting under argon atmosphere. Table 1 shows the wt% nominal chemical composition of both alloys. First, commercially obtained ZK40 and Ag were melted at 750 °C in a steel crucible and held for 30 min with continuous stirring and later cast into billets. The cast ingots were hot extruded with an extrusion ratio of 15.6 using a die heated at 350 °C to produce 27.5 mm × 27.5 mm square cross-section billets. In an attempt to solutionize the as-extruded billets and homogenize the grain structure, a long duration heat treatment of 350 °C for 7 days in Argon atmosphere was performed.

Microstructure

Microstructures of the as-extruded and solution-treated billets were observed using optical microscopy. EDM machined, disc-shaped samples with ~1.7 cm^2 cross-sectional area were mounted in cold-curing epoxy resin and grinded using silicon carbide paper up to 1200 grit. Polishing of the samples was done using 3 μm and 1 μm diamond suspensions. The polished surfaces were washed with ethanol and dried with air.

Table 1 The nominal wt% chemical compositions of ZK40 and ZK40–Ag

Alloy	Composition (wt%)					
	Zinc	Zirconium	Silver	Manganese	Calcium	Magnesium
ZK40	4.7	0.35	<0.01	0.01	N/A	Remainder
ZK40–Ag	4.89	0.18	2.56	0.01	0.01	Remainder

Specimens were etched using acetic-picral solution (4.2 g picric acid, 70 ml ethanol, 10 ml acetic acid and 10 ml distilled water).

Mechanical Properties

Cylindrical samples of 3 mm diameter and 6 mm in length were used for compression testing. Tests were performed at ambient temperature and conducted at an initial strain rate of 10^{-3}/s using electromechanical MTS Insight 30 kN machine. The load cell used was 5 kN and testing was done in triplicates. Vickers micro-hardness tests were conducted as well with a load of 100 gf and a dwell time of 15 s.

Electrochemical Tests

Electrochemical tests were conducted using a Gamry Multiport™ three-electrode cell: the sample acted as the working electrode, a graphite rod was used as a counter-electrode and Ag/AgCl as a reference electrode. Similar samples to those used for microstructural analysis were used for EIS, however the samples were grinded up to 800 SiC grit on all sides before mounting. This is to prevent crevice corrosion occurring between the sample and the epoxy. Prior to mounting as well, an insulated wire was attached to the back of the specimen to provide the electrical connection to perform the electrochemical testing. One surface of the sample was exposed by grinding up to 1200 SiC and then immersed into 1000 ml of Hank's solution at 37 °C. The pH of the solution was maintained at 7.4 using 0.1 M HEPES [4-(2-hydroxyethyl)-1-piperazineethanesulfonic acid] buffering solution. The experiments were conducted for a total of 24 h using Electrochemical Impedance Spectroscopy (EIS) by sweeping the frequency between 10^5 and 10^{-2} Hz at 10 mV AC amplitude. Open circuit potential (OCP) was measured in parallel with EIS at different time points to observe the change in corrosion behavior with respect to time. Potentiodynamic polarization (PD) was also carried out at the end of the testing period at a scanning rate of 1 mV/s from −2.5 to +0.5 V.

Results and Discussion

Microstructure Analysis

Figure 1 shows optical micrographs of ZK40 before and after heat treatment at 350 °C for 7 days along two orthogonal planes i.e. transverse plane (TP) and extrusion plane (EP). In the as-extruded ZK40, the microstructure along transverse plane is similar to what has been observed in other extruded Mg alloys [29–31]. The as-extruded microstructure contains long, elongated grains (LEG) oriented along the extrusion direction, in addition to two other types of grains: fine equiaxed grains (FEG) and row stacked grains (RSG) that can also be observed. Azeem et al. and others have reported that among these three types of grains, LEGs are reminiscent of the as-cast microstructure and FEGs are

Fig. 1 Microstructure of the two orthogonal planes for ZK40 before and after heat treatment (TP—Transverse Plane and EP—Extrusion Plane)
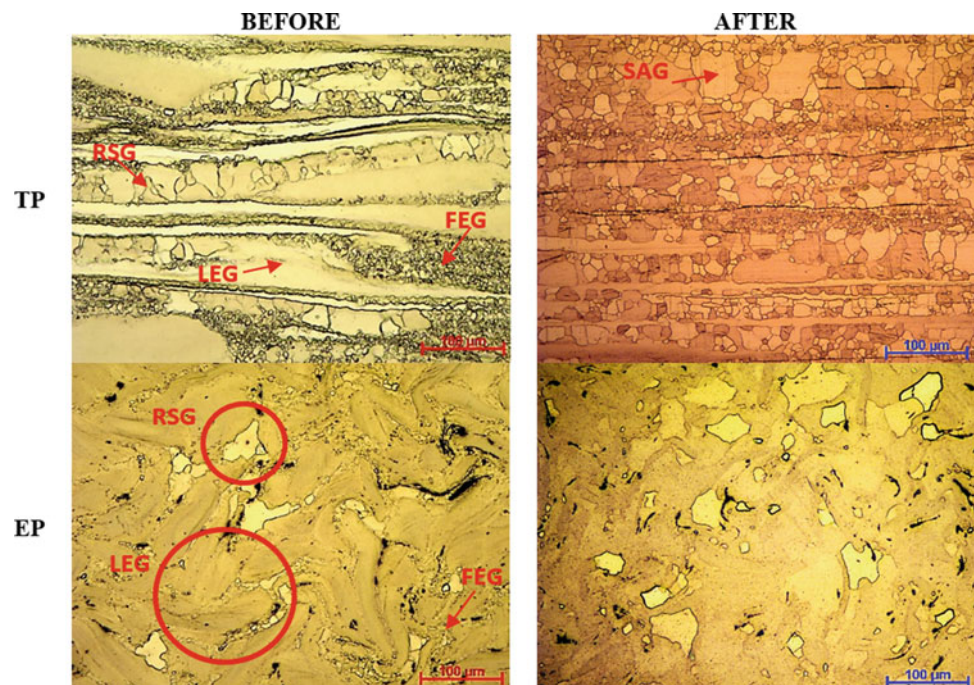
dynamically recrystallized grains (DRX), while RSGs are misaligned grains that have undergone DRX but at a lower rate due to their misalignment [32]. Aligned grains are those that have their basal plane aligned with the extrusion direction, which is one of the most common slip systems for deformation in Mg [33]. The plastic energy stored in misaligned grains is lower than that of the aligned grains, therefore they recrystallize at a lower rate resulting in bands of large recrystallized grains stacked in a row-like structure [32].

Apart from the Mg matrix, the presence of other Zn–Zr rich phases in the microstructure seen as dark streaks along the extrusion direction was confirmed by a preliminary Energy Dispersive X-ray Spectroscopy (EDX) analysis (Fig. 2). After heat treatment, the LEGs recrystallize but thinner LEGs are still observed throughout the microstructure. Also, some reduction in the distribution of Zn–Zr rich phases is seen, however, the long-duration heat treat regime did not fully solutionize them. Furthermore, an overall homogenization of the grain structure is observed as well as an increase in the grain size of FEGs.

In case of the extrusion plane of ZK40 (Fig. 1), the grain morphologies that were observed in the transverse plane are not easily distinguishable. Some LEGs are visible as large grains and swirling outlines of Zn–Zr-rich phases are observed along the LEG grain boundaries as well as dark particles within the grains. FEGs are seen as small, fine equiaxed grains while RSGs are shown as coarser grains, both smaller in grain size than LEGs. Post-heat treatment, the decrease in volume fraction of Zn–Zr rich phases are apparent and grain sizes seem to have homogenized and increased due to static recrystallizaion (RX), as seen in the transverse plane.

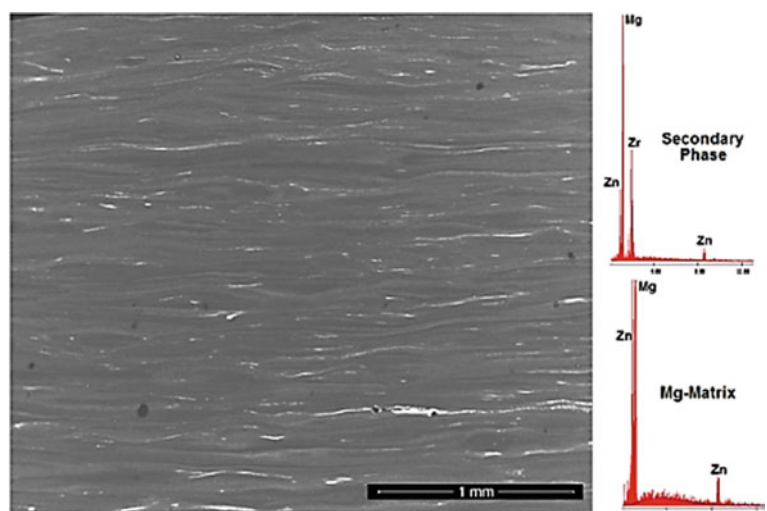Optical micrographs of ZK40–Ag before and after heat treatment are shown in Fig. 3. Prior to the heat treatment, the addition of 2 wt% Ag resulted in an increase in the volume fraction of secondary phases as presented by the darker and thicker streaks in the transverse plane which is reflected by large, sized dark patches in the extrusion plane. Furthermore, the composition of the secondary phases is altered, as shown by EDX analysis in Fig. 4, and the grain structure is more homogenous now with smaller, equiaxed grains which can be observed in both planes. Ben-Hamu et al. reported similar findings when 1, 2, and 3 wt% Ag was added to Mg–6Zn alloy [28]. The smaller grain size in ZK40–Ag, compared to ZK40, could be explained by the constricting of grain growth and DRX that normally occur during extrusion as a result of the increased volume fraction of the secondary phases [34].

Similar to ZK40, heat treatment of the ZK40–Ag alloy resulted in an agglomerated morphology of secondary phases and an increase in grain size but the effect was significantly more pronounced. The secondary phase agglomeration is apparent in the transverse plane micrograph by the thicker, more disperse dark streaks oriented along the extrusion direction as opposed to the extrusion plane. From the microstructures, in Figs. 1 and 3, it was concluded that the main effect of Ag on microstructure was the aggregation of secondary phases in addition to an increase in their volume fraction. Furthermore, the grain size distribution was more homogenous with Ag addition compared to the as-extruded ZK40 condition.

Mechanical Properties

The mechanical properties of as-extruded and heat-treated ZK40 and ZK40–Ag alloys were investigated through microhardness measurements and compression tests (Figs. 5 and 6). It was observed that in ZK40, extrusion plane

Fig. 2 BSE micrograph of the transverse plane and EDX spectrum of as-extruded ZK40
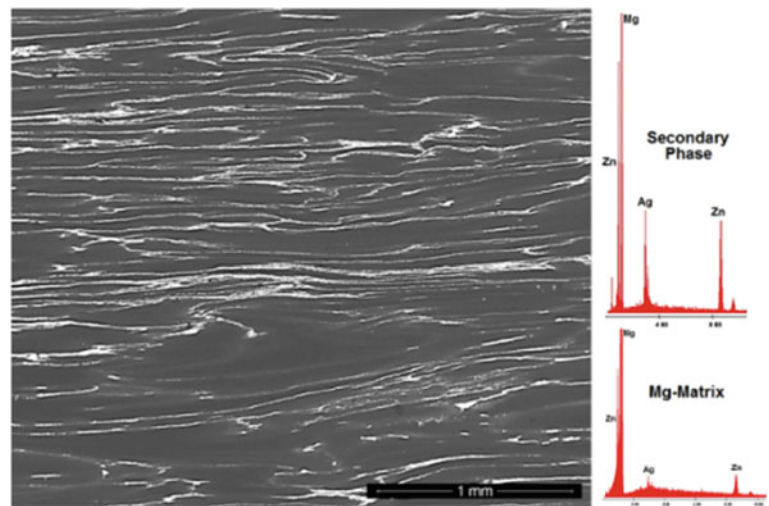
Fig. 3 Microstructure of the two orthogonal planes for ZK40–Ag before and after heat treatment
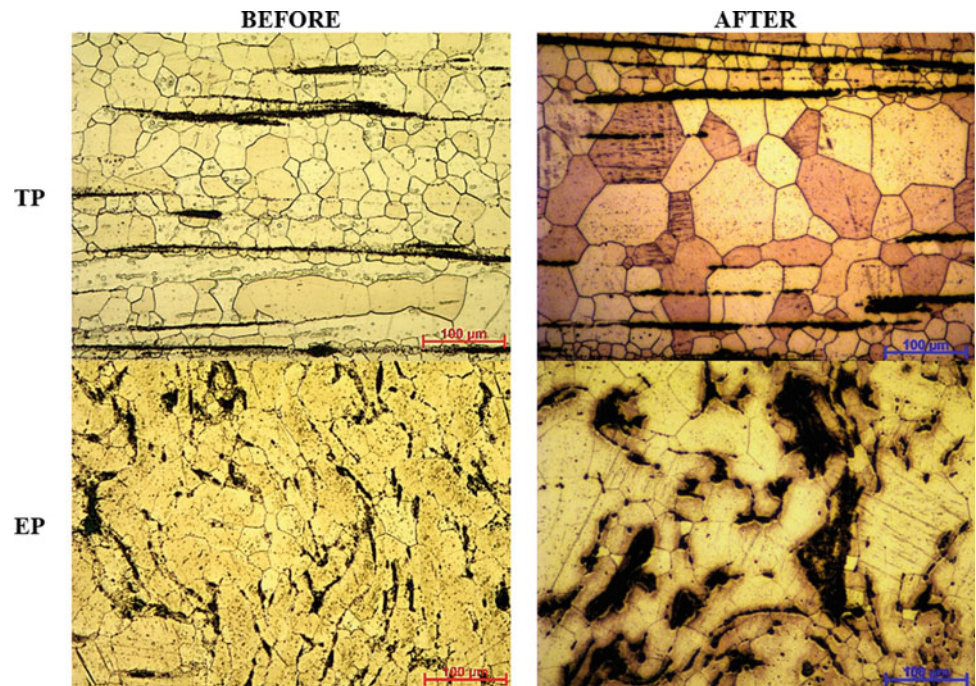

**Fig. 4** BSE micrograph of the transverse plane and EDX spectrum of as-extruded ZK40–Ag

exhibited higher hardness than transverse plane while in ZK40–Ag transverse plane exhibited higher hardness than extrusion plane. Among the two alloys, ZK40–Ag displayed higher microhardness than ZK40 in the transverse plane while it displayed less hardness in the extrusion plane. Mandal et al. reported that adding 0.1 at.% of Ag to Mg–2.4Zn alloy resulted in an increase in hardness of about 20 HV for the as-cast homogenized condition, due to secondary phase precipitation [35]. This is in agreement with the trend observed in the transverse plane between ZK40 and ZK40–Ag. However, the increase in HV was not as significant as that reported by Mandal et al. which could be due to the larger grain size observed in ZK40–Ag after solutionizing as

larger grain sizes tend to counteract the hardening benefits of precipitates [28].

In contrast, the extrusion plane of ZK40–Ag displayed less hardness than ZK40. It is worthwhile to note that microhardness measurements were taken within the matrix while excluding the precipitates. In an effort to investigate the decrease in microhardness of ZK40–Ag, measurements of the precipitates were taken and their average was found to be 130 HV, which is more than double the hardness values of the Mg matrix. Furthermore, since Ag resulted in the aggregation of the secondary phases, particularly in the extrusion plane, the volume fraction of secondary phases within the matrix would be less. Therefore, a decrease in the
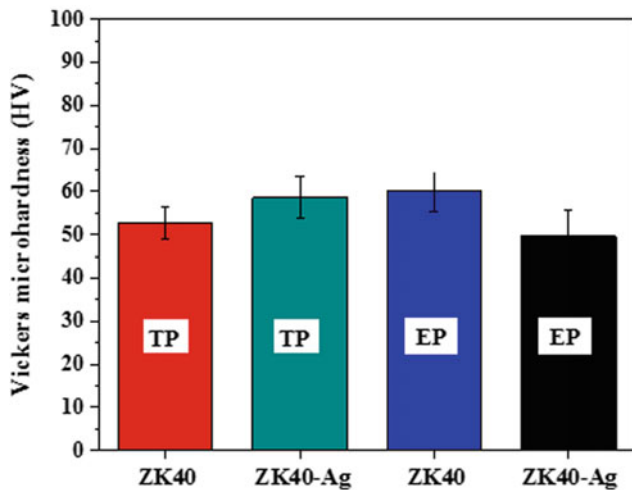
Fig. 5 Effect of Ag addition on Vicker's microhardness of ZK40 in the two orthogonal planes
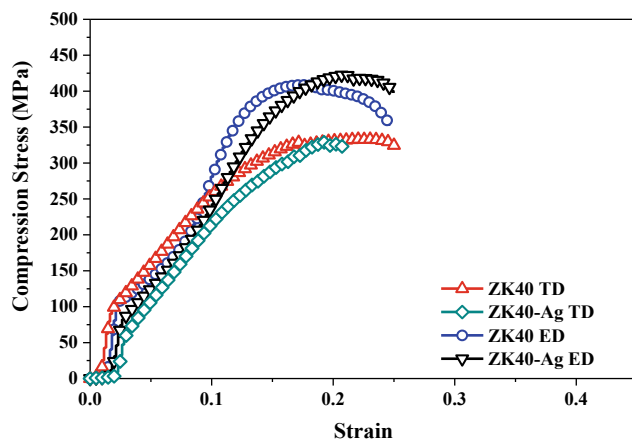
Fig. 6 Stress–strain curves of ZK40 and ZK40–Ag at room temperature under compressive loading applied along with the two orthogonal directions (TD—Transverse Direction and ED—Extrusion Direction)

hardness of the matrix is perhaps expected. There may be other factors that lead to this microhardness trend reversal in ZK40–Ag compared to ZK40 such as Zn depletion of the Mg matrix due to Ag-rich precipitates which is observed while comparing the EDX spectrum of the matrices of both alloys in Figs. 2 and 4.

Figure 6 shows the compression stress-strain curves of ZK40 compared to ZK40–Ag along with the two orthogonal directions, i.e., transverse and extrusion directions. In ZK40, the ultimate compressive strength in the extrusion direction was higher compared to the transverse direction with similar ductility observed in both planes. Looking back at the microstructures, the comparatively homogenized grain structure and absence of LEGs in the extrusion plane led to an increased compressive strength which was similar to the microhardness results in Fig. 5. A similar trend was also

observed in the ZK40–Ag with the extrusion direction showing higher values of compressive strength than the transverse direction. Of all the directions tested, the highest compressive strength was observed for ZK40–Ag in the extrusion direction which is opposite to the trend observed in the microhardness measurements (Fig. 5). The agglomeration of the secondary phases as well as the depletion of Zn into the matrix could explain why the overall hardness of the ZK40–Ag was less in the extrusion plane but still had a positive impact on the compressive strength of the alloy, Further investigation is needed to fully understand the role of secondary phases and grain structure on the mechanical properties of both alloys.

Open Circuit Potential

The reactivity of a metal surface can be determined based upon the open circuit potential (OCP) of the alloy throughout the immersion time. The OCP of both alloys in the transverse and extrusion planes is presented in Fig. 7. Both orthogonal planes of ZK40 experienced a decrease in their potential after their first few hours of immersion, while an increase was observed towards the end of the 24 h. The OCP for the extrusion plane specifically continued to increase steadily after the small drop during the initial hours, which implies that the surface film of the extrusion plane is able to maintain its integrity throughout the testing period, although it is at a lower potential than the transverse plane. ZK40–Ag OCP curve shows a plateau which is at a more positive potential than ZK40. This is expected since the addition of Ag causes an increase in secondary phases and as reported
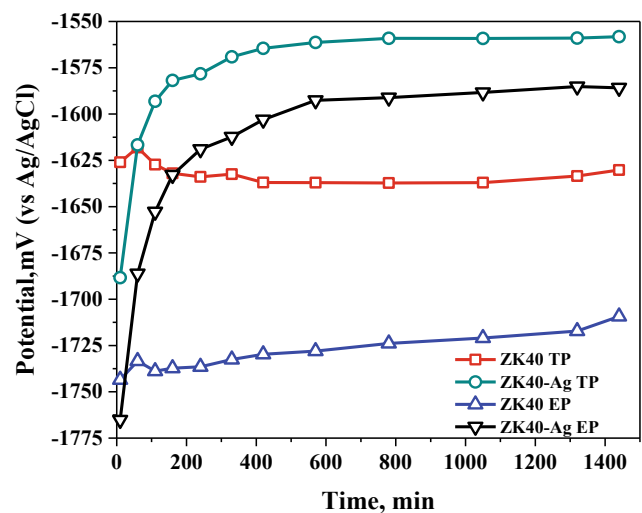
Fig. 7 Open circuit potential (OCP) of ZK40 and ZK40–Ag at 37 °C throughout 24 h of immersion in Hank's solution for both transverse (TP) and extrusion (EP) planes

by Gusieva et al., Ag is more noble than Mg [36]. During the initial few minutes of immersion, the OCP of ZK40–Ag in transverse plane experienced the sharpest increase which indicates the increased stability of the surface film being formed. ZK40 transverse plane also reached the same OCP value of around 1615 mV which also shows that the film-forming on the surface of ZK40 transverse is stable as well. After 24 h of immersion, both OCPs of ZK40–Ag have reached a plateau and therefore signifying the continuous breaking down of the developed surface film. The alloy, however, is still presenting higher potential than ZK40 and

that is a result of the higher volume fraction of secondary phases present that are cathodic to the matrix. Consequently, microgalvanic cells were formed between the matrix and the secondary phases, thereby causing corrosion of the matrix. Since most of the Ag was found in the secondary phases and Ag is nobler than Mg, the presence of Ag continued to be enhanced as the matrix was continuously being compromised. This explains why the plateau occurred at a more positive potential for both planes of ZK40–Ag compared to the planes of ZK40. As immersion time increased, the slopes for all OCP started to decrease indicating that the developed films were losing their integrity and breaking down.
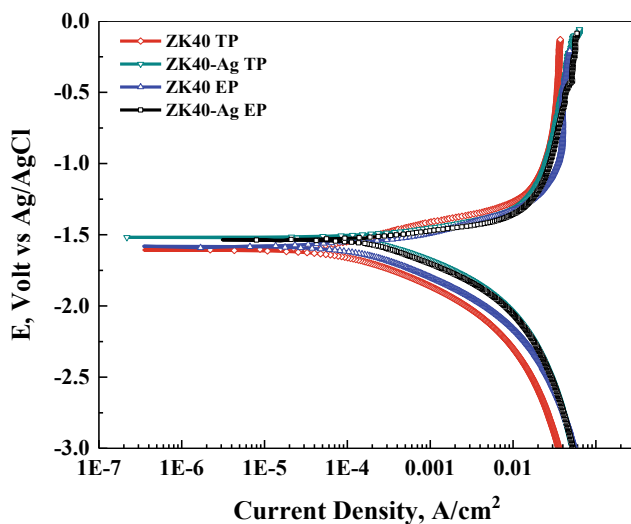
Fig. 8 Potentiodynamic curves of ZK40 and ZK40–Ag at 37 °C after 24 h of immersion in Hank's solution for both transverse (TP) and extrusion (EP) planes

Potentiodynamic Polarization Curves

The potentiodynamic (PD) curves of ZK40 and ZK40–Ag in the transverse and extrusion planes are shown in Fig. 8. In both planes, ZK40–Ag displayed a more positive potential than ZK40 which is in agreement with the OCP results. This was also consistent with the ennobling effect of Ag as reported by Mandal et al. where the addition of Ag resulted in a shift in the corrosion potential towards a more positive value [35]. Furthermore, the intersection between the anodic and cathodic branch, which is an indication of the corrosion rate occurs at a higher corrosion current, i_{corr}, when Ag is added compared to no Ag addition. Gusieva et al. presented similar results where the increased addition of Ag resulted in an increase in cathodically controlled kinetics and a more positive E_{corr} value, which increased the value of i_{corr} [37]. The increase in corrosion current led to an increase in corrosion rate which is in agreement with EIS results presented in Fig. 9.
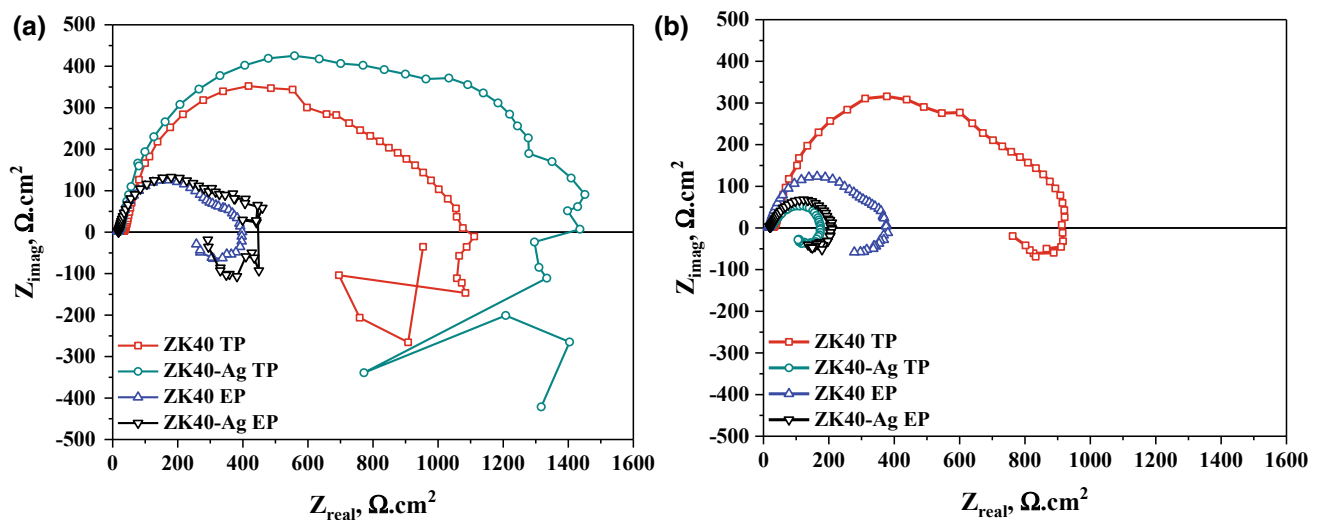
Fig. 9 Nyquist plots of ZK40 and ZK0–Ag at 37 °C after **a** 1 h of immersion and **b** 24 h of immersion in Hank's solution for both transverse (TP) and extrusion (EP) planes

Electrochemical Corrosion Measurements

Electrochemical Impedance Spectroscopy (EIS) is a technique that investigates the processes occurring at the metal surface using AC polarization [38]. The EIS Nyquist plots for ZK40 and ZK40–Ag immersed in Hank's solution at 37 °C for 1 and 24 h for both planes are presented in Fig. 9. All plots are distinguished by two capacitive loops at high and medium frequencies and an inductance loop at low frequencies. The trends seen in both plots are in accordance with the results observed in OCP plots. After the first hour of immersion, the transverse planes for ZK40 and ZK40–Ag both exhibited a significant increase in corrosion resistance which is evident with the large diameter of the capacitive loop. However, by the end of the experimental period, both planes of ZK40 had a higher corrosion resistance than both planes of ZK40–Ag. The drastic decrease in the corrosion resistance of the alloy with Ag addition is due to the enhanced microgalvanic corrosion caused by the larger volume fraction of secondary phases as observed in Figs. 1 and 3. Furthermore, as was observed in Fig. 7, the corrosion resistance of ZK40 in the extrusion plane experienced minimal, if no change at all, throughout the 24 h of immersion. Further analysis using circuit fittings could give some insight on the reasons behind this behavior.

Another interesting observation that was also noticed is that overall the transverse plane experienced much better corrosion resistance than the extrusion plane. Considering the microstructure of both alloys that are shown in Figs. 1 and 3, the extrusion plane has a more homogenous, fine-grained structure and smaller grains especially in ZK40. A homogenous grain structure has been reported to present improved protection against corrosion because of its ability to form a more stable corrosion layer [39, 40]. However, in this case the structure of the matrix is not the only factor influencing the corrosion behavior of the alloy. The volume fraction and distribution of the secondary phases also play an important role in determining how the alloy would behave in corrosive environments. The microstructures of the transverse planes for ZK40 and ZK40–Ag (Figs. 1 and 3, respectively) show that the distribution of the secondary phases are sparse and are interconnected to form dark streaks. Zhang et al. reported that discontinuous secondary phases have a detrimental effect on the corrosion resistance of Mg–Nd–Zn–Zr as they studied the influence of increasing Ag addition (0, 0.2, 0.4 and 08 wt%) [39]. The distribution of secondary phases in extrusion plane for both alloys, on the other hand, is disconnected and is dispersed throughout the matrix. Post-immersion microstructures are necessary to be able to confirm these observations.

Conclusions

The following are the conclusions of this work:

1. Microstructure analysis revealed that the addition of silver followed by a heat treatment of 350 °C for 7 days resulted in a homogenized microstructure with larger grain size. Furthermore, the composition and distribution of secondary phases were altered and their volume fraction increased. Both the transverse and extrusion planes showed the same trends.

2. Addition of silver led to an increase in hardness between the transverse planes of ZK40 and ZK40–Ag but a decrease in hardness measurements in the extrusion plane. A contradictory result was observed during compression where an increase in compressive strength in the extrusion plane was noted while the transverse plane barely witnessed any change in strength. This is could be due to the shape and distribution of secondary phases as well as their composition. Further analysis will aid in explaining these results.

3. ZK40–Ag presented a more positive OCP than ZK40 independent of the plane being tested. This was attributed to the increased volume fraction of secondary phases that have a more positive potential than the α-Mg matrix due to the presence of Ag. During the initial hours of immersion, the transverse planes for both alloys showed a more stable surface film. However, as immersion time increased, the developed films in both planes for ZK40–Ag seemed unable to maintain their integrity in comparison with ZK40.

4. PD results show that the addition of Ag resulted in an increase in cathodically controlled kinetics and a more positive E_{corr} value, therefore causing an increase in i_{corr} values and corrosion rates.

5. EIS results were in agreement with PD and OCP results. After the first hours of immersion, the transverse planes for ZK40 and ZK40–Ag both exhibited a significant increase in corrosion resistance, however, by the end of the testing period, ZK40 presented improved corrosion resistance than ZK40–Ag. This is in agreement with the literature stating that Ag has a negative effect on the corrosion characteristics of Mg alloys.

6. This work lays the foundation to understanding the role of microstructural features, as a result of Ag addition, on the mechanical and corrosion characteristics of Mg alloys. The authors plan to apply severe plastic deformation to a suitable system in the future to further improve the properties presented herein.

References

1. Chen Y, Xu Z, Smith C, Sankar J (2014) Recent advances on the development of magnesium alloys for biodegradable implants. Acta Biomater 10:4561–4573. https://doi.org/10.1016/j.actbio.2014.07.005

2. Wang J, Smith CE, Sankar J, et al (2015) Absorbable magnesium-based stent: physiological factors to consider for in vitro degradation assessments. Regen Biomater 2:59–69. https://doi.org/10.1093/rb/rbu015

3. Staiger MP, Pietak AM, Huadmai J, Dias G (2006) Magnesium and its alloys as orthopedic biomaterials: A review. Biomaterials 27:1728–1734. https://doi.org/10.1016/j.biomaterials.2005.10.003

4. Li X, Liu X, Wu S, et al (2016) Design of magnesium alloys with controllable degradation for biomedical implants: From bulk to surface. Acta Biomater 45:2–30. https://doi.org/10.1016/j.actbio.2016.09.005

5. Witte F, Kaese V, Haferkamp H, et al (2005) In vivo corrosion of four magnesium alloys and the associated bone response. Biomaterials 26:3557–3563. https://doi.org/10.1016/j.biomaterials.2004.09.049

6. Zhao D, Witte F, Lu F, et al (2017) Current status on clinical applications of magnesium-based orthopaedic implants: A review from clinical translational perspective. Biomaterials 112:287–302. https://doi.org/10.1016/j.biomaterials.2016.10.017

7. Ding Y, Wen C, Hodgson P, Li Y (2014) Effects of alloying elements on the corrosion behavior and biocompatibility of biodegradable magnesium alloys: a review. J Mater Chem B 2:1912–1933. https://doi.org/10.1039/C3TB21746A

8. Gawlik MM, Wiese B, Desharnais V, et al (2018) The effect of surface treatments on the degradation of biomedical Mg alloys-a review paper. Materials (Basel) 11:1–29. https://doi.org/10.3390/ma11122561

9. Ratna Sunil B, Sampath Kumar TS, Chakkingal U, et al (2016) In vitro and in vivo studies of biodegradable fine grained AZ31 magnesium alloy produced by equal channel angular pressing. Mater Sci Eng C 59:356–367. https://doi.org/10.1016/j.msec.2015.10.028

10. Minárik P, Král R, Čížek J, Chmelík F (2016) Effect of different c/a ratio on the microstructure and mechanical properties in magnesium alloys processed by ECAP. Acta Mater 107:83–95. https://doi.org/10.1016/j.actamat.2015.12.050

11. Saha P, Roy M, Datta MK, et al (2015) Effects of grain refinement on the biocorrosion and in vitro bioactivity of magnesium. Mater Sci Eng C 57:294–303. https://doi.org/10.1016/j.msec.2015.07.033

12. Buzolin RH, Mohedano M, Mendis CL, et al (2017) As cast microstructures on the mechanical and corrosion behaviour of ZK40 modified with Gd and Nd additions. Mater Sci Eng A 682:238–247. https://doi.org/10.1016/j.msea.2016.11.022

13. Yuan Y, Ma A, Jiang J, et al (2013) Optimizing the strength and ductility of AZ91 Mg alloy by ECAP and subsequent aging. Mater Sci Eng A 588:329–334. https://doi.org/10.1016/j.msea.2013.09.052

14. Mokhtarishirazabad M, Azadi M, Hossein Farrahi G, et al (2013) Improvement of high temperature fatigue lifetime in AZ91 magnesium alloy by heat treatment. Mater Sci Eng A 588:357–365. https://doi.org/10.1016/j.msea.2013.09.067

15. Lu Y, Bradshaw AR, Chiu YL, Jones IP (2015) Effects of secondary phase and grain size on the corrosion of biodegradable Mg–Zn–Ca alloys. Mater Sci Eng C 48:480–486. https://doi.org/10.1016/j.msec.2014.12.049

16. Zhang S, Zhang X, Zhao C, et al (2010) Research on an Mg-Zn alloy as a degradable biomaterial. Acta Biomater 6:626–640. https://doi.org/10.1016/j.actbio.2009.06.028

17. Mostaed E, Vedani M, Hashempour M, Bestetti M (2014) Influence of ECAP process on mechanical and corrosion properties of pure Mg and ZK60 magnesium alloy for biodegradable stent applications. Biomatter 4:e28283. https://doi.org/10.4161/biom.28283

18. Song X, Chang L, Wang J, et al (2018) Investigation on the in vitro cytocompatibility of Mg-Zn-Y-Nd-Zr alloys as degradable orthopaedic implant materials. J Mater Sci Mater Med 29. https://doi.org/10.1007/s10856-018-6050-8

19. Guan RG, Cipriano AF, Zhao ZY, et al (2013) Development and evaluation of a magnesium-zinc-strontium alloy for biomedical applications - Alloy processing, microstructure, mechanical properties, and biodegradation. Mater Sci Eng C 33:3661–3669. https://doi.org/10.1016/j.msec.2013.04.054

20. Vinogradov A, Vasilev E, Kopylov V, et al (2019) High Performance Fine-Grained Biodegradable Mg-Zn-Ca Alloys Processed by Severe Plastic Deformation. Metals (Basel) 9:186. https://doi.org/10.3390/met9020186

21. Chen D, He Y, Tao H, et al (2011) Biocompatibility of magnesium-zinc alloy in biodegradable orthopedic implants. Int J Mol Med 28:343–348. https://doi.org/10.3892/ijmm.2011.707

22. AbdelGawad M, Mansoor B, Chaudhry AU (2018) Corrosion Characteristics of Two Rare Earth Containing Magnesium Alloys BT - Magnesium Technology 2018. In: Orlov D, Joshi V, Solanki KN, Neelameggham NR (eds). Springer International Publishing, Cham, pp 43–53

23. AbdelGawad M, Chaudhry AU, Mansoor B (2019) The Influence of Temperature and Medium on Corrosion Response of ZE41 and EZ33. In: Joshi VV, Jordon JB, Orlov D, Neelameggham NR (eds) Magnesium Technology 2019. Springer International Publishing, Cham, pp 159–167

24. Hong D, Saha P, Chou DT, et al (2013) In vitro degradation and cytotoxicity response of Mg-4% Zn-0.5% Zr (ZK40) alloy as a potential biodegradable material. Acta Biomater 9:8534–8547. https://doi.org/10.1016/j.actbio.2013.07.001

25. Song G (2005) Recent progress in corrosion and protection of magnesium alloys. Adv Eng Mater 7:563–586. https://doi.org/10.1002/adem.200500013

26. Tie D, Feyerabend F, Hort N, et al (2014) In vitro mechanical and corrosion properties of biodegradable Mg-Ag alloys. Mater Corros 65:569–576. https://doi.org/10.1002/maco.201206903

27. Kannan MB, Raman RKS (2008) In vitro degradation and mechanical integrity of calcium-containing magnesium alloys in modified-simulated body fluid. Biomaterials 29:2306–2314. https://doi.org/10.1016/j.biomaterials.2008.02.003

28. Ben-Hamu G, Eliezer D, Kaya A, et al (2006) Microstructure and corrosion behavior of Mg-Zn-Ag alloys. Mater Sci Eng A 435–436:579–587. https://doi.org/10.1016/j.msea.2006.07.109

29. Zhang X, Yuan G, Niu J, et al (2012) Microstructure, mechanical properties, biocorrosion behavior, and cytotoxicity of as-extruded Mg-Nd-Zn-Zr alloy with different extrusion ratios. J Mech Behav Biomed Mater 9:153–162. https://doi.org/10.1016/j.jmbbm.2012.02.002

30. Minárik P, Král R, Pešička J, et al (2016) Microstructure characterization of LAE442 magnesium alloy processed by extrusion and ECAP. Mater Charact 112:1–10. https://doi.org/10.1016/j.matchar.2015.12.002

31. Mostaed E, Hashempour M, Fabrizi A, et al (2014) Microstructure, texture evolution, mechanical properties and corrosion behavior of ECAP processed ZK60 magnesium alloy for biodegradable applications. J Mech Behav Biomed Mater 37:307–322. https://doi.org/10.1016/j.jmbbm.2014.05.024

32. Azeem MA, Tewari A, Mishra S, et al (2010) Development of novel grain morphology during hot extrusion of magnesium AZ21 alloy. Acta Mater 58:1495–1502. https://doi.org/10.1016/j.actamat.2009.10.056

33. Song GL (2012) The effect of texture on the corrosion behavior of AZ31 Mg alloy. Jom 64:671–679. https://doi.org/10.1007/s11837-012-0341-1

34. Ben-Hamu G, Eliezer D, Shin KS (2006) Influence of Si, Ca and Ag addition on corrosion behaviour of new wrought Mg-Zn alloys. Mater Sci Technol 22:1213–1218. https://doi.org/10.1179/174328406X109203

35. Mandal M, Moon AP, Deo G, et al (2014) Corrosion behavior of Mg-2.4Zn alloy micro-alloyed with Ag and Ca. Corros Sci 78:172–182. https://doi.org/10.1016/j.corsci.2013.09.012

36. Gusieva K, Davies CHJ, Scully JR, Birbilis N (2015) Corrosion of magnesium alloys: the role of alloying. Int Mater Rev 60:169–194. https://doi.org/10.1179/1743280414Y.0000000046

37. Gusieva K, Sato T, Sha G, et al (2013) Influence of low level Ag additions on Mg-alloy AZ91. Adv Eng Mater 15:485–490. https://doi.org/10.1002/adem.201200321

38. Kirkland NT, Birbilis N, Staiger MP (2012) Assessing the corrosion of biodegradable magnesium implants: A critical review of current methodologies and their limitations. Acta Biomater 8:925–936. https://doi.org/10.1016/j.actbio.2011.11.014

39. Zhang X, Ba Z, Wang Z, et al (2013) Influence of silver addition on microstructure and corrosion behavior of Mg-Nd-Zn-Zr alloys for biomedical application. Mater Lett 100:188–191. https://doi.org/10.1016/j.matlet.2013.03.061

40. Lin DJ, Hung FY, Liu HJ, Yeh ML (2017) Dynamic Corrosion and Material Characteristics of Mg–Zn–Zr Mini-Tubes: The Influence of Microstructures and Extrusion Parameters. Adv Eng Mater 19:1–11. https://doi.org/10.1002/adem.201700159